Scanning Microscopy

Volume 2 | Number 3 Article 12

4-25-1988

Multiphoton Ionization Followed by Time-of-Flight Mass Spectroscopy of Sputtered Neutrals

M. J. Pellin
Argonne National Laboratory

C. E. Young
Argonne National Laboratory

D. M. Gruen
Argonne National Laboratory

Scanning Microscopy, Vol. 2, No. 3, 1988 (Pages 1353-1364)
Scanning Microscopy International, Chicago (AMF O'Hare), IL 60666 USA

MULTIPHOTON IONIZATION FOLLOWED BY TIME-OF-FLIGHT MASS SPECTROSCOPY OF SPUTTERED NEUTRALS*

M. J. Pellin, C. E. Young, and D. M. Gruen*

Materials Science and Chemistry Divisions
Argonne National Laboratory
Argonne, IL 60439-4831

(Received for publication April 13, 1987, and in revised form April 25, 1988)

Abstract

Multiphoton ionization (MPI) by pulsed, tunable lasers provides a sensitive means for detection of neutral atoms, resulting from the high probability achievable in both the ionization and subsequent detection steps. Substantial selectivity is achieved by excitation between energy levels of the atom of interest. This resonant MPI technique can access all atomic states including ground and metastable levels.

The high efficiency of MPI technique permits detailed sputtering data to be obtained with minimal target damage. The goal is to obtain velocity and angular distributions for each energy level of every sputtered species. In practice, two types of experimental configurations have been employed. In one method, the photoionized atoms are allowed to strike a spatially resolved detector near the target, with extraction fields that preserve the angular distribution information. Velocity information is obtained by time of flight (TOF). This method is most suitable for majority species in the sputtered flux. In the case of minority species (either very dilute surface constituents or highly excited states produced), additional noise reduction is necessary. A suitable configuration involves extraction of the photoions into a sector-field TOF mass spectrometer. In standard, isochronous operation, energy and angular spreads at the point of ionization are compensated in flight to produce sharp TOF mass spectra. Noise sources (photons, metastable and scattered atoms) escaping through transparent grids are strongly suppressed. Angular distributions can be mapped "pointwise" by varying the relation between the point of ion beam impact and the photoionization volume. Velocity data can be obtained from the TOF spectra or by Doppler scanning on any resonant step of the laser excitation. Recent data are discussed.

Key words: Multiphoton ionization (MPI), multiphoton resonance ionization (MPRI), resonance ionization spectroscopy (RIS), laser secondary neutral mass spectrometry (LSNMS), useful yield, sputtering, time-of-flight (TOF), mass spectrometry, isochronous, refocusing, laser ionization, nonresonant ionization, post ionization, ultrasensitive detection.

*Address for correspondence:
D.M. Gruen, MSD/CHM 200,
Argonne National Laboratory, 9700 S. Cass Ave.
Argonne, IL 60439-4831
Phone No. (312) 972-3513

Introduction

Laser multiphoton ionization of sputtered atoms has proven to be a sensitive probe both for studies of the sputtering process (16, 17, 30, 59) and of surface composition (5 - 8, 14, 29, 31, 38, 39, 40, 43-45, 65). This laser-based ionization version of secondary neutral mass spectrometry (LSNMS) has several advantageous features. First, laser ionization techniques measure the dominant fraction of the sputter flux which for metals and semiconductors are neutral atoms (32). Second, because the dominant neutral portion of the sputter flux is measured, large changes in signal due to minor surface chemical effects may be minimized (46, 47). It shall be pointed out, however, that there are instances when neutral atoms do not represent the dominant portion of the sputtered flux, such as when oxygen is absorbed on the surface in the presence of extended sputtering (28) or for oxide materials (14). Finally, in the case of resonance ionization spectroscopy (RIS), the laser ionization process is so species specific (67) that the requirement for a mass spectrometer of high resolution, and therefore poor transmission, is alleviated.

A comparison of LSNMS to other sputtered neutral mass spectrometric (SNMS) techniques such as that of Oechsner et al. (37) has been drawn previously (49) based on their relative ionization efficiency, the range of species ionized, and the experimental duty cycle. In this paper, a more detailed comparison of the various LSNMS techniques will be drawn and a few of the most exciting new results will be reviewed.

Basically, LSNMS represents an extremely efficient though low-duty cycle ionization method. For sufficiently large laser powers, most elements may be ionized with unit efficiency. This can be compared to electron ionization efficiencies (35) of $\cong 0.01\%$ and hot electron gas efficiencies (37) of 1%. For most SNMS techniques, the ionization efficiency is reasonably mass independent (49). For LSNMS the ionization can be species unspecific (nonresonant) or very species specific (resonant). Finally, one must consider the duty cycle of the experiment. While most SNMS techniques operate with unit duty cycle, the LSNMS duty cycle is limited by the laser repetition rate of commercially available pulsed lasers to 10^{-4}, constituting a significant disadvantage for routine analysis.

This paper will focus on two important quantities for surface analysis - the useful yield, Ψ, and the bulk sensitivity limit. The useful yield is defined

as:

$$\Psi = \text{atoms detected/atoms sputtered}$$

This important quantity represents the key limit for microcharacterization of samples with atomic dimensions, e.g., surface monolayers.

The bulk sensitivity limit of a technique represents a different type of sensitivity. In the overall context of materials analysis, it might be better characterized as near surface analysis. Several factors play a role in this limit. In the case of duty cycle limited experiments such as LSNMS, there is essentially no difference between sample limited (surface) analysis and near surface analysis. For the more conventional SNMS techniques (35, 37) and for secondary ion mass spectroscopy (SIMS), duty cycle is not a limiting problem. In these cases, the bulk sensitivity limit is a function of the signal-to-noise ratio of the measurement without regard to sample consumption. The signal-to-noise ratio will be enhanced for successively longer averaging times until the bulk sensitivity limit is reached. Often this limit is due to an isobaric interference. In the best cases, this limit arises from detector dark current.

Useful Yield, Ψ

Let us examine in detail the useful yield, Ψ for LSNMS technique which may be defined as follows:

$$\Psi = \Psi_a \Psi_{ms} \qquad (1)$$

where Ψ_{ms} is the mass spectrometer transmission factor for photoions created in the laser photoionization region and Ψ_a is the fraction of sputtered atoms which are photoionized. Ψ_a is a function of the laser spot size and position, the laser ionization efficiency, the primary ion pulse width, the relative timing of the laser and ion pulses, the sputtered atom velocity distribution, and for resonant ionization the excited electronic state distribution of the sputtered flux. Let us examine Ψ_a and Ψ_{ms} in turn.

An understanding of Ψ_a can be obtained by starting with the simplest case. Figure 1 presents a detailed two-dimensional projection of the photoionization region. Let us first consider ε, the fraction of sputtered atoms in the photoionization volume which depends on the number density velocity distribution of sputtered atoms. At any given time, t_L, following the end of the primary ion pulse, there will exist atoms with velocities both too large and too small to be in the photoionization volume. The magnitude of this effect can be estimated by assuming that the targets of interest sputter as predicted by linear collision cascade theory (55-58). These theories derive the energy distribution of the flux of sputtered atoms by assuming that each primary ion impact is independent and produces an isotropic collision cascade of target atoms. This Sigmund-Thompson collision cascade theory has proved remarkably accurate for all measured sputtered ground state atom distributions (3, 4, 9, 13, 15-17, 19, 21-27, 30, 42, 52, 53, 59-64). This E^{-2} energy distribution of colliding atoms is refracted at the surface by a surface binding energy, E_b, leading to a flux energy distribution of sputtered atoms of:

$$f(w,\theta)d\Omega dw = [\cos\theta\, d\Omega/\pi]\ [2wdw/(1+w)^3] \qquad (2)$$

where $w\ (=E/E_b)$ is a reduced energy parameter and θ is the angle shown in Fig. 1. The factors in square brackets are chosen to integrate to unity. Since the geometry of interest assumes a small volume element and since we are interested in determining the optimum laser firing delay, t_L, this flux energy distribution must be transformed into the following number density velocity distribution:

$$g(u)d\Omega du = (\pi/2v_b)\ [d\Omega/2\pi]\ [(16/\pi)\ .\ u^2du/(1+u^2)^3] \qquad (3)$$

where $u(=v/v_b = w^{1/2})$ is the reduced velocity parameter and $v_b\ [=(2E_b/m)^{1/2}]$ can be found from the binding energy. The number density velocity distribution, g(u), is displayed in Fig. 2. As a result of the velocity vector dependent flux to number density transformation, g(u) is independent of θ and peaks at lower u values than does the flux density velocity distribution. The above distributions, f and g, apply to the steady state case where the target is continuously bombarded. In practice, the bombardment needs to be maintained for a time sufficient for the slowest atoms of interest to reach the probing volume.

For an arbitrarily short primary ion pulse, however, there exists a one-to-one correspondence between g(u) and the number density of sputtered atoms along the target normal at any given time, t, following the primary ion pulse. Atom density is probed by the laser in a fixed volume $dV = R^2 d\Omega dR$ at position R after time-of-flight t. The signal may be assigned to the variable u by the relation $uv_bt = R$. The corresponding density of atoms, n(u,R), per atom released in the short pulse is given by:

$$n(u,R) = (1/R^3)\ [\cos\theta/\pi]\ \{4u^4/(1+u^2)^3\}. \qquad (4)$$

There exists a time, $t_L = R/2^{1/2}v_b$, for which ε is maximized. The crosshatched region of Fig. 2 represents the fraction of atoms which are located at a distance between 0.5 mm and 1.5 mm from the target along the target normal at t_L. This represents nearly 60% of all the sputtered atoms.

Three conclusions are immediately evident from this simplistic analysis. First, a large fraction of all sputtered atoms are available for photoionization. Second, the optimum delay time between the primary ion pulse striking the target and the laser firing time, t_L, is different (although with a weak dependence) for each atomic mass. Finally, a more complete analysis including the three-dimensional laser volume and ion pulses of finite time width is necessary.

In order to examine analytically these two effects on ε, let us return to Fig. 1 and assume that the laser volume is a cylinder of height (z_2-z_1) and of radius h. For this case, g(u) can be integrated to find ε for an arbitrary primary ion pulse width and for any t_L. This solution is analytic in the two cases - of either long and very short primary ion pulses. First consider short ion pulses followed by a time t_L. In this case:

$$\varepsilon = [\cos(\theta)d\Omega/\pi]\ [4u^4/(1+u^2)^3\ dR/R] \qquad (5)$$

where R is the distance from the target to the ionization volume center and $R^2dRd\Omega$ defines an infinitesimal volume element. For the finite cylindrical volume, the previous equation can be integrated using $z = R\cos\theta$, $R = ua$, and $a = v_bt_L$, to give:

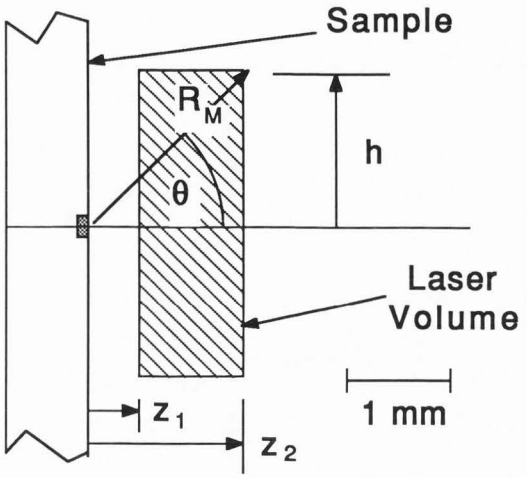

Fig. 1. Detailed drawing of the laser ionization region. z_1 and z_2 represent the spatial extent of the laser beams, ϕ is the target normal referenced ejection angle of sputtered atom, and h the largest off-axis distance over which photoions may be collected by the detection optics. The 1 mm distance provides the reader with a typical scaling factor.

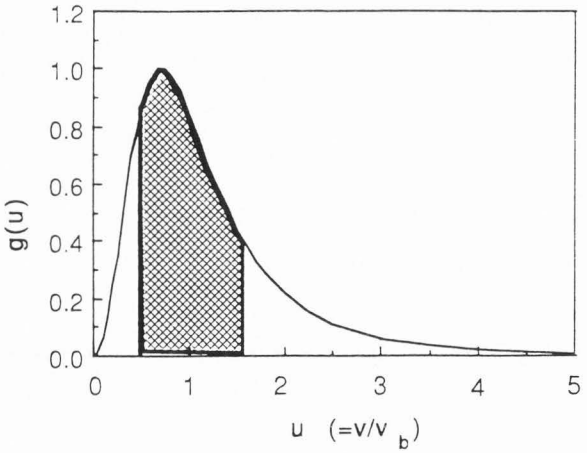

Fig. 2. Depicted is the number density velocity distribution of atoms sputtered with a Sigmund-Thompson energy distribution. In the limit of a delta function primary ion pulse, there exists a one-to-one correspondence of points on this curve and the number density of atoms at a given distance from the target. U represents the reduced velocity (= v/v_b). The crosshatched region represents the fraction of atoms which are between 0.5 and 1.5 mm from the target for a delta function primary ion pulse at a time t_L.

$$\varepsilon = p(z_1) - p(z_2) \qquad (6)$$

where $p(z) = a^2/(a^2+z^2) - a^2/(a^2+h^2+z^2)$ can be found by inserting the parameters for each of the instruments being compared here.

While the shortest primary ion pulses result in the largest ε's, the shortest ion pulse is not necessarily the optimum experimental condition. This conundrum arises from the limited duty cycle of laser-based experiments. Consider a primary ion pulse of 0.1 pCoulombs. This is clearly close to the delta function limit for pulses of peak currents in the μamp range. For materials with a sputtering yield of 1, there exist only 2.6×10^5 atoms in the SARISA (which stands for "surface analysis by resonance ionization of sputtered atoms") photoionization volume. In an experiment with a 100 Hz repetition rate, it would take many seconds to remove even one atom of a ppb impurity.

The necessity of using longer primary ion pulses in order to accomplish impurity maps in a more reasonable time frame leads us to an examination of the next analytical solution for ε - the long pulse limit. The fundamental assumption made in deriving this equation is that the primary ion pulse is so long that all velocities have uniformly distributed themselves across the photoionization region. In this case the efficiency, in a differential volume element, is:

$$\varepsilon = [\cos(\theta)d\Omega/\pi]\ [\pi dR/4v_b\tau] \qquad (7)$$

where τ is the primary ion pulse length. Again, for the finite cylindrical volume of Fig. 1:

$$\varepsilon = [q(z_2)-q(z_1)] \qquad (8)$$

where $q(z) = z\ \{1-[1+(h/z)^2]^{\frac{1}{2}}\}$. Rigorously, the long pulse assumption would require an infinitely long (continuous) primary ion pulse ($\tau = \infty$). Of course the efficiency for this case is 0. In practice, however, since the low velocity portion of the sputtered number density velocity distribution (Fig. 2) represents a relatively small fraction of the total sputtered number density velocity distribution, a minimum duration can be found for primary ion pulse times, τ, as follows:

$$\tau = (R_M/u^*)\ (1/v_b) \qquad (9)$$

where u^* is v^*/v_b. The quantity v^* can be defined as the lowest velocity which will traverse the distance R_M (Fig. 1) during τ. The optimum time, t_L, for firing the laser pulse will typically occur slightly after τ (so that the volume acquires slightly more slow atoms, while escaping fast ones are still being replenished). Thus the assumption of uniformly distributed atom velocities in the photoionization volume is rigorously true for all velocities greater than v^*. For $u^* = 0.6$, nearly 80% of all sputtered atoms fall in this limit. For Fe atoms sputtered from an Fe surface, $u^* = 0.6$ implies $\tau = 0.92$ μs giving $\varepsilon = 0.20$. Even in the worst case limit (no atoms sputtered with a velocity less than v^* in the photoionization volume), $\varepsilon = 0.16$.

It is apparent that in this more complete three-dimensional description the fraction of photoionizable sputtered atoms decreases somewhat when compared to the simplest one-dimensional case but remains a sizeable fraction of the total sputtered flux. In fact not all of the atoms which are irradiated in the laser volume become ions. The reason for this is different in the case of resonant ionization and nonresonant ionization. Let us examine the ionization efficiency, θ, for each of these cases in turn.

While, in principle, any atom may be resonantly photoionized, it is useful to consider a particular element, Fe. The energy level diagram of gas phase

Fe atoms is displayed in Fig. 3. For resonant ionization, two (43-45, 65) or even three (38, 40) lasers may be used in the photoionization process. In Fig. 3 the two-color ionization process is displayed in which ground state Fe atoms are first resonantly excited using the $y^5D_4^o \leftarrow a^5D_4$ transition at 302.065 nm and then are ionized with a 308 nm photon. The second step in the ionization of Fe involves a bound-free transition which typically requires laser intensities in the 10-100 MW/cm^2 range to be efficient. However, many commercial pulsed lasers are available which can easily supply saturating laser intensities even for the relatively large laser-irradiated volumes employed by SARISA.

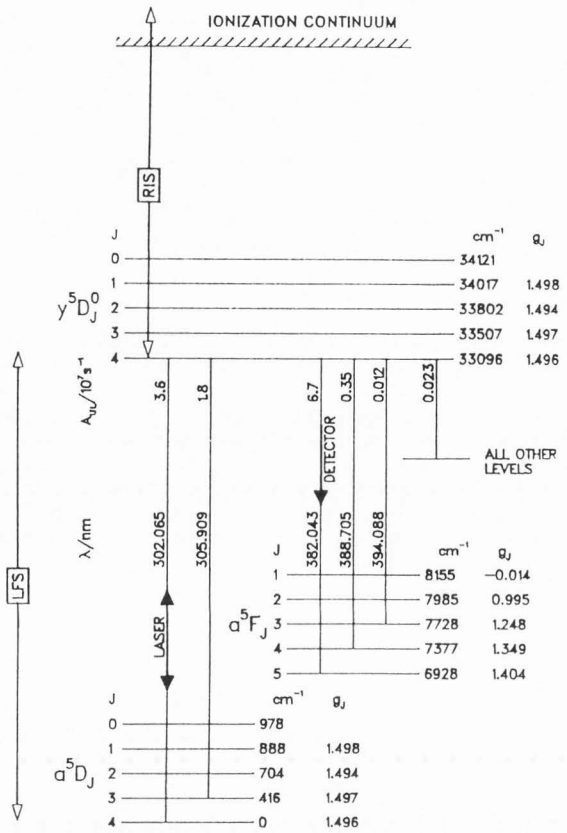

Fig. 3. An Fe atom energy level diagram showing the transitions used for resonant ionization of sputtered Fe atoms.

Figures 4 and 5 describe SARISA saturation studies of the resonant and ionizing lasers used in the photoionization of Fe atoms. The studies were conducted using clipped Gaussian profile laser beams in order to eliminate the effective laser interaction region volume changes normally associated with changes in laser intensity (12). Furthermore, MPI was accomplished with two separate lasers - a dye laser operating at 302.065 nm and a XeCl excimer operating at 308 nm. Independent adjustment of the laser intensities is crucial for careful saturation studies since the transition dipole moment for resonant excitation can be orders of magnitude larger than for transitions to the ionization continuum. The ionization process can be characterized by an overall efficiency parameter, ρ. The saturation studies (Figs. 4 and 5) demonstrate that effectively all ground state Fe atoms in the laser volume could be photoionized with relatively moderate laser powers ($\rho = 1$) and that the resonant laser intensity required was nearly one order of magnitude smaller than the ionizing laser intensity. This becomes important since various saturation phenomena such as power broadening and Stark shifts can actually decrease the photoionization efficiency with increasing intensity (1).

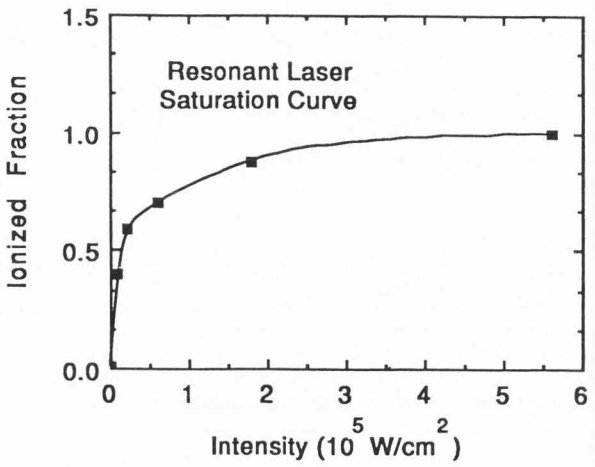

Fig. 4. Fe^+ signal as a function of resonant laser intensity for a SARISA measurement of Fe atoms sputtered from a Si matrix. Note that saturation is achieved for moderate laser intensities.

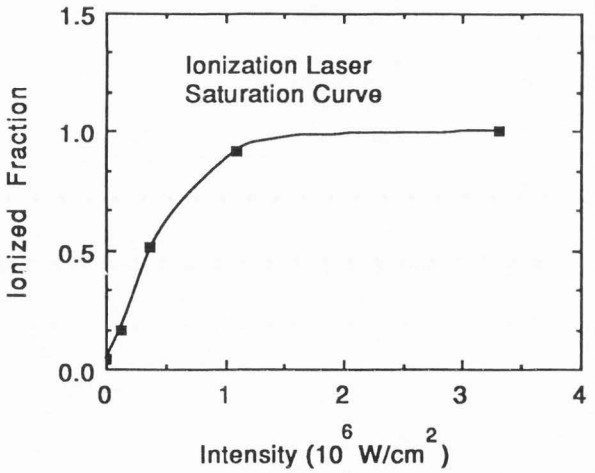

Fig. 5. Fe^+ signal as a function of ionizing laser intensity for a SARISA measurement of Fe atoms sputtered from a Si matrix. Note that saturation of the ionization laser signal requires substantially higher laser intensities than for the resonant step.

The ground state ionization efficiency of resonant multiphoton ionization can be one for nearly every element. However the sputtering process does not leave all the atoms in the ground electronic state. For instance, for iron nearly 40% of the

sputtered atoms are in excited states (3, 4, 15-17, 21, 43-45, 52, 53, 65) with most of this population in excited fine structure levels of the ground state. The fraction of excited atoms has been measured for a number of systems (16, 17, 41). In all cases the ground state fraction has been > 0.5. For atoms such as Li which sputter from high work function matrices with large ion fractions, laser ionization will be only of limited advantage.

The situation for nonresonant multiphoton ionization is somewhat different. Nonresonant ionization accesses all molecules and atoms regardless of excited state with varying efficiencies. The excitation efficiency is largely sample independent and must be calibrated as a function of laser intensity. Figure 6 is a SARISA saturation measurement for Cu atoms and Cu_2 molecules sputtered from a polycrystalline Cu surface. In this experiment only one nonresonant laser color was used (308 nm). Clearly saturation is not reached. This is a function of the laser color and intensity. The relatively large laser cross section used in SARISA in order to maximize ε makes saturation difficult to achieve for many atomic and molecular species.

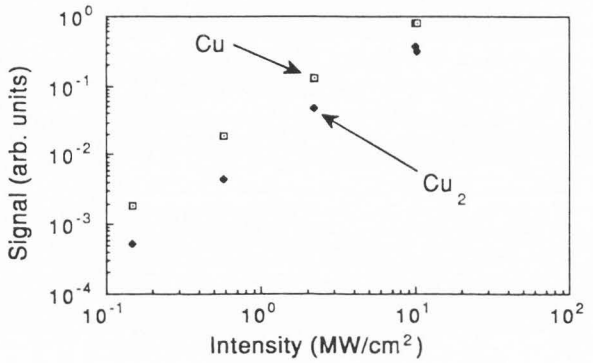

Fig. 6. Intensity dependence of the SARISA Cu^+ and Cu_2^+ photoion signal for nonresonant multiphoton ionization with 308 nm light. The Cu atoms and molecules were sputtered by 3.7 keV Ar^+ primary ions from a polycrystalline Cu surface.

Nonresonant excitation will photoionize neutral atoms in all electronic energy levels. Thus to first order, excited state distributions of sputtered atoms are of no concern. However, elements with large secondary ion yields will have effectively lower ρ 's. Ψ_a can now be found as the product of ρ and ε. For large laser volumes, it seems possible that Ψ_a 's in the range 0.05 to 0.15 can routinely be achieved with resonant excitation. For nonresonant excitation, saturation in many cases will require smaller laser volumes, and Ψ_a 's of 0.01 to 0.03 are achievable.

This examination has up until now focused basically upon the possible signal available in LSNMS experiments. Clearly trace analysis requires rejection of large numbers of noise ions in order to achieve meaningful measurements. For resonant ionization experiments, substantial noise rejection is accomplished in the photoionization process. Several noise sources, including secondary ions of the bulk material, high energy backscattered primary ions and laser-created nonresonant ions, remain. In nonresonant MPI, all the noise rejection must be accomplished in the mass spectrometer with the advantage that all elements in the sample are detected essentially simultaneously.

A system, which displays excellent noise rejection and in which useful yields Ψ = 0.1 have been demonstrated, will be described in the next section.

Surface Analysis by Resonance Ionization of Sputtered Atoms (SARISA)

The SARISA apparatus consists of four major subunits - the ion source, the sample vacuum chamber, the energy and angle refocusing time-of-flight (EARTOF) mass spectrometer, and the ionizing lasers. The vacuum chamber routinely achieves 10^{-10} Torr base pressures and includes an Auger electron spectrometer, a LEED system, and a residual gas analyzer.

The primary ion beam was generated by a Colutron source which was both differentially pumped and mass analyzed. For all the work reported here, 3.5 keV Ar^+ was used as the primary ion beam. The source produced an average current of up to 3 μA in a 250 μm FWHM spot on the target. Depth profiles were produced with ion milling of a Lissajous rastered spot of 2 mm by 2 mm dimension. During SARISA impurity analysis, the ion beam was directed into the center of the ion-milled region and then temporally chopped into 2 μs pulses by deflection across one of the differential pumping apertures. The pulse of primary ions is carefully synchronized with the 20 Hz laser repetition rate.

Two lasers are used to ionize the sputtered atoms. The resonant laser was a Nd:YAG-pumped dye laser (Molectron MY34/DL-18) whose frequency-doubled output was tuned to match a resonant transition of the impurity of interest. The excited atom is then ionized by absorption of a photon from a second laser. This laser is a XeCl excimer laser (Lumonics #TE-860) which produces light with a 0.3-0.5 nm bandwidth about 307.9 nm. For Fe and most metallic atoms, this two-photon absorption scheme (one resonant and one ionizing) is sufficient to excite the atom above its ionization potential ultimately producing an ion.

The EARTOF spectrometer is shown schematically in Fig. 7. A key feature is the einzel lens operation at high negative potential in the vicinity of the target with the consequence that (1) the primary ion beam is focused onto the sample with minimum aberration, and (2) laser-produced photoions are extracted with high efficiency while their energy-spread due to the draw-out potential in the laser volume is held to an acceptably small value. A second important design improvement has been the introduction of sector-electric-field deflection elements into the flight path of the product ions, allowing isochronous TOF operation, i.e., compensation of the overall flight times of photoions for the variation induced by distributions in initial energy and direction of the sputtered atoms. The improvement in mass resolution results directly in additional suppression of noise, since detection gates can be narrowed without attendant loss of signal. Basic principles of energy/angle isochronous TOF have been discussed previously (48), and recently a comprehensive analysis of the design principles of such devices has been given and tested (50, 51). As will be indicated

in the detailed discussion below, the present apparatus takes advantage of the isochronous refocusing principle while retaining a simplicity of fabrication for the individual components.

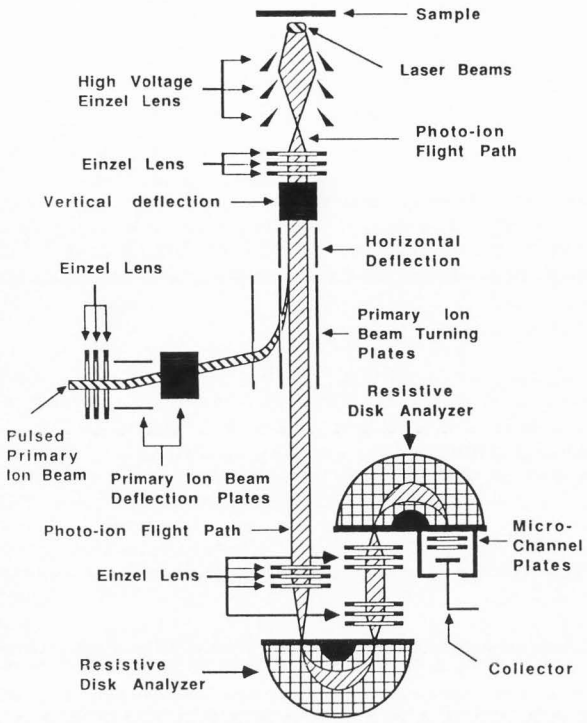

Fig. 7. The SARISA Energy and Angle Refocusing Time-of-Flight (EARTOF) system for detection of sputtered neutral atoms. The element labels are self-explanatory. A detailed description of the instrument operation may be found in the text.

The critical region adjacent to the sample is depicted in Fig. 8. The extraction electrode configuration is shown with a typical axial electrostatic potential indicated in Fig. 9. The three-element group adjacent to the target is operated at high negative potential (-21 kV) in order to focus the primary ion beam onto the sample. The electrode directly adjacent to the target (Fig. 8) was given the sharp-edged conical shape in order to minimize redeposition problems. As Liebl has pointed out in the context of SIMS (34), it proved impossible to collimate returning low-energy ions (of the same charge sign as the primaries) without the aid of an additional lens. The same situation applies in the case of photoions, produced in a volume near the surface. A triple aperture lens at lower potential (-2.8 kV) was employed as a photoion collimator while having little effect on the high energy primary beam.

Particle optics properties of the extraction lens system were determined via ray-tracing with the aid of the program EGUN (20). The EGUN numerical code generates electrostatic potentials, given the electrode boundary conditions. Subsequently, ion trajectories are calculated for a variety of starting conditions. In regions of cylindrical symmetry, the code gives both spatial orbit and flight time for each ray. Flight paths through the 180° spherical sectors are in a region of lower symmetry than cylindrical but their exact analytical formulas are possible for both the orbits and times of flight (33). By combining analytical expressions and numerical code data, a value for the total transit time from the laser volume to the detector is obtained.

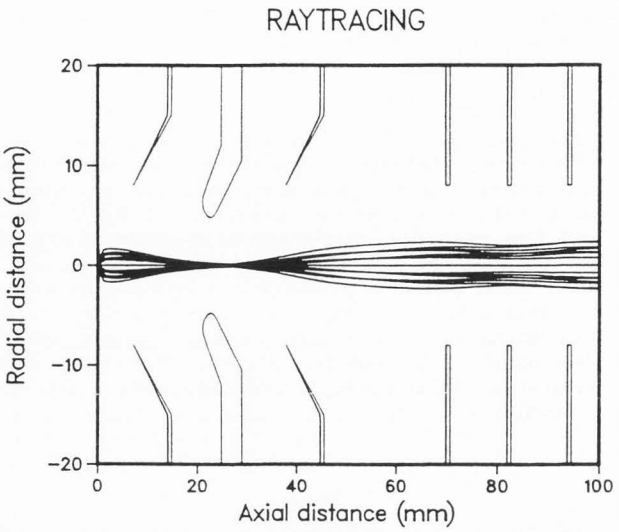

Fig. 8. Electrodes and typical photoion trajectories. Sample, extraction and collimation region.

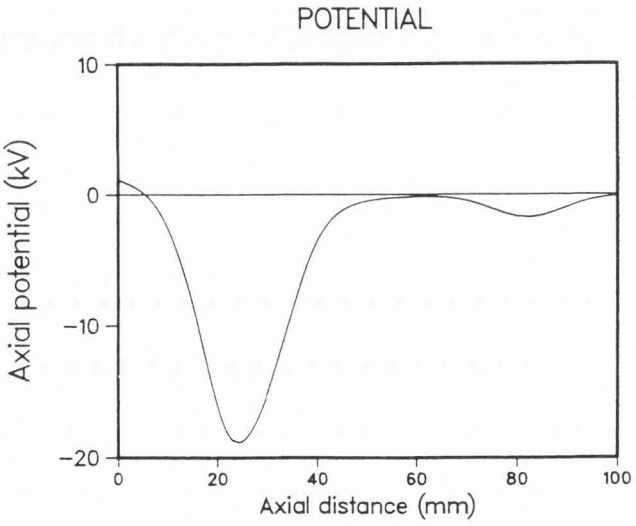

Fig. 9. Axial potential.

Since the positive time dispersion in the spherical sectors ($dt/dT > 0$, t = time, T = initial kinetic energy) is opposite to that on near-linear flight paths, a stationary value of the flight time can be achieved relative to variations in initial kinetic energy of ions in the laser volume. The condition is achieved by proper selection of flight path dimensions and is optimized experimentally by a trim adjustment of the nominal potential in a portion of the linear flight path. The angular refocusing property of the spherical sectors is also necessary to achieve

high resolution. With two 180° units, coupled by a focal imaging, a full 360° path results and the same flight time accrues independent of the sign of any initial angular deviation. Large-gap spherical deflector devices are constructed to utilize exact boundary-matching in the region between spherical conductors by means of current flow in resistive materials (54). An outer electrode of highly transparent metal mesh has been found advantageous for allowing the escape of potential noise sources (e.g., scattered ions, electronically excited metastables).

The large extraction fields required for efficient photoion collection result in substantial energy variation across the laser volume (152 V for the conditions of Fig. 10). The spread in photoion energies thus induced dominates that due to the energy width characteristic of sputtering. Potential energy variation near the target is quite linear, however, and optimization of machine parameters for isochronous operation relative to initial ion position in the laser volume results in an experimental mass resolution of 200.

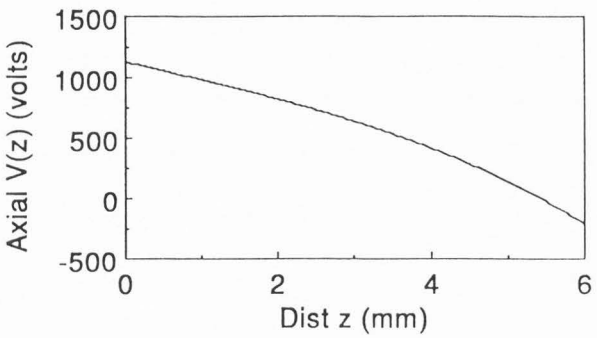

Fig. 10. Detail of laser ionization region. Near-linear potential in laser volume.

A complete description of the operation of this apparatus requires reference to the experimental timing sequence displayed in Fig. 11. It is the pulsed nature of the experiment which allows the combination of high throughput and high noise immunity. The data collection sequence is initiated with a 2 μs - long ion pulse which traverses the set of deflection plates and then passes through the primary ion turning plates which merge the primary ions onto the EARTOF axis by means of electrostatic deflection. The beam then is focused onto the target by the high voltage ion lens. As can be seen in Fig. 11, the primary ion pulse strikes the sample target during a time when the sample is held at a high potential (1400 V). 300 ns following the end of the primary ion pulse, the target potential is lowered to 1100 V and the two lasers are triggered. The photoions are generated in a spatial region which extends from 0.5 mm to 1.5 mm above the target surface. The radial dimensions of this volume are of order 2 mm. Once created, the photoions are accelerated away from the target and into the EARTOF by the large potential field of the target. These photoions then traverse the high voltage lens region. Because of the unique lens design, the photoions are then focused through the primary ion turning plates and onto the entrance aperture of the first resistive disk analyzer. The two resistive-disk energy analyzers are spherical energy analyzers which are constructed to have large angular and energy acceptance windows. This is accomplished using boundary electric field matching conditions as already discussed (54).

The combination of two spherical analyzers provides two key functions for the SARISA EARTOF. First, they strongly suppress the high energy noise ions which were produced during the sputtering process and then ejected when the target was held at high potential. Second, since the photoions were extracted with a large energy spread (1000 ± 100 V), the dual analyzer is necessary to improve the TOF mass resolution.

Following traversal of the two spherical energy analyzers, the photoions strike a chevron pair of microchannel plates. The subsequent electron pulse is then detected either by a gated pulse-counting system or by a multichannel charge digitizer depending on signal levels.

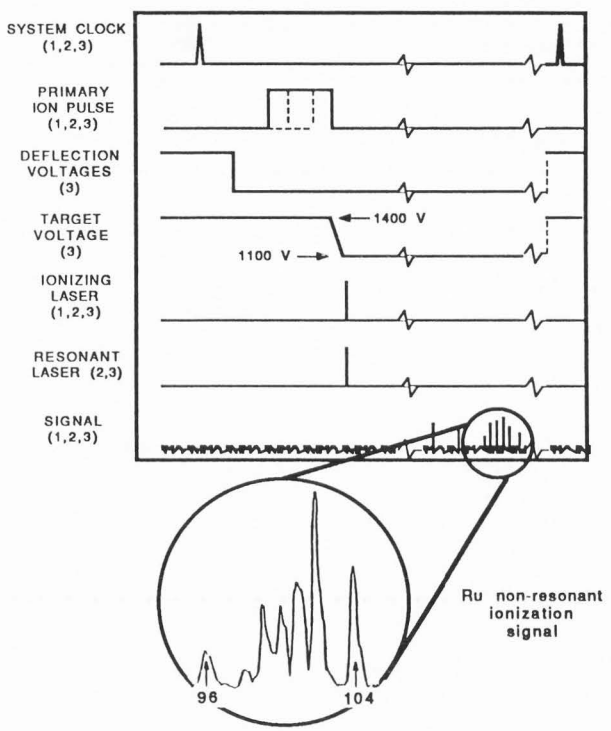

Fig. 11. SARISA timing diagram.

Useful Yield, Ψ, for LSNMS as Exemplified by SARISA Measurements

The sensitivity of the SARISA apparatus was determined using an Fe^{56} implanted Si wafer. TRIM code computer simulations (11, 18) of the expected depth profile for this implantation reveal a 400 ppb peak Fe^{56} atomic concentration at a depth of about 50 nm. SIMS depth profiles of 60 keV Fe^{54} implanted Si samples also have this characteristic profile. SIMS studies of Fe^{56} could not be directly compared because the isobaric Si_2 limited depth profiling sensitivities to ~1 ppm (J. M. Anthony, private communication).

Figure 12 illustrates the Fe concentration of the Fe^{56} implanted Si wafer as determined by the

SARISA apparatus. The Fe^{56} levels were calibrated by fixing the peak concentration at the expected 400 ppb level. Similar levels were found by calibration with SARISA determination of Fe sputtered from a pure Fe target. This calibration uses the known Fe sputtering yield and assumes that Fe sputters from the Si substrate with the same yield as Si from Si (i.e., S = 1.4)(2, 36). It is also necessary to include a slight change in the fraction of Fe in the ground electronic state with changing matrix (43-45, 65).

An evaluation of the number of counts detected at this depth leads to a determination of the total transmission of the SARISA apparatus for Fe^{56}. The useful yield in terms of photoions detected/atoms sputtered was 5% in this experiment. Since RIS measures only ground state atoms, it is useful to apply the known ground state fraction (43-45, 65) to calculate a 9% yield of photoions detected/ground state Fe^{56} sputtered. This can be compared to the calculated 17% of sputtered Fe^{56} which we calculate to be in the laser volume during the laser ionization process (66).

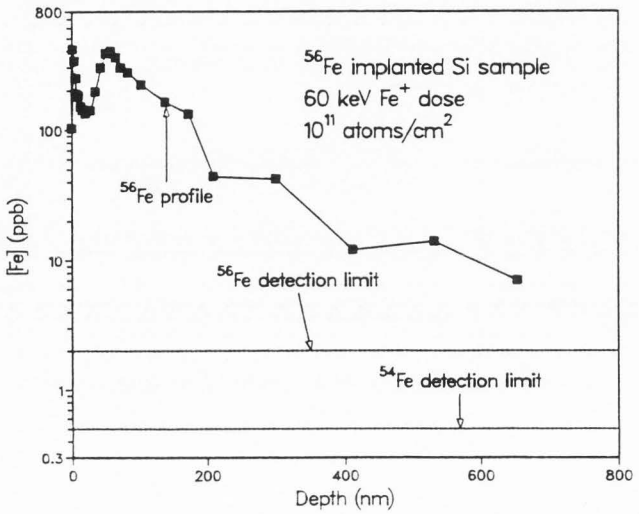

Fig. 12. SARISA depth profile of ^{56}Fe implanted Si (III). A 60 keV, 10^{11} atoms/cm^2 implantation dose was used to prepare the sample. The ^{56}Fe and ^{54}Fe detection limits are the calculated impurity limits for a signal-to-noise ratio of 1. Each measurement is made with removal of 0.5 of a monolayer.

These samples have an oxide layer which is approximately 6 nm thick. Therefore for finding the depth scale and the Fe yield in this layer, we have used the SiO_2 sputtering yield (10) which is 1. At this point, there is an abrupt drop in the Si^+ yield. Interestingly, there is very little change in the Fe RIS signal at this point. Clearly, the yield of ground state Fe is quite insensitive to the Si oxidation state in contradistinction to the situation found in dynamic oxidation sputtering experiments (28).

The experimental method with which the data in Fig. 12 were taken is somewhat different from that used in conventional SIMS and requires some explanation. The lines are drawn to aid the eye, the symbols representing separate SARISA impurity determinations. The statistical error associated with each measurement is smaller than the symbol itself. The material removed in each measurement was, in all cases, less than 20% of a monolayer. In between SARISA determinations, the ion beam was directed onto the target in a continuous fashion. Deflection plates were used to produce a 2 mm by 2 mm raster pattern in order to mill away the sample and avoid crater wall effects.

A close examination of Fig. 12 reveals an interesting variation of the Fe^{56} concentration in the near surface region. Within the first monolayer of the surface, the Fe^{56} concentration reveals a relatively low value of 110 ppb. Only a few atomic layers deeper, the concentration rises dramatically. This near surface peak fluctuated as a function of position on the implanted Si wafer. We feel that the surface peak represents Fe contamination introduced during the implantation process due perhaps to the stainless steel walls and apertures of the ion implanter used.

While the last Fe^{56} measurement reveals an impurity concentration of 8±2 ppb, it is legitimate to ask what the detection limit is for a signal-to-noise level of 1. Given a 2 μA peak current in a 2 μs pulse with a 0.25 mm dia. spot, half a monolayer would be removed after 10,000 pulses and the detection limit would be 2 ppb. The detection limit is not lower because of background from nonresonant ionization of neutral Si_2. Our laser ionization scheme is relatively simple. Additional discrimination from nonresonant ionization of isobaric components has been demonstrated to occur in double resonance experiments (67). To assess the ultimate limits of sensitivity, we conducted experiments (not shown) on the signal in the Fe^{54} time window. For clean Si substrates under good ultrahigh vacuum conditions, a detection limit of 500 ppt was determined under the experimental conditions described above. Interestingly, for experiments done with a base pressure of 3 x 10^{-9}, this detection limit degraded to a measured 1 ppb value due to an increase in secondary ions and molecular sputtering.

The sensitivity of the LSNMS technique in general and SARISA in particular will clearly be able to address certain analytical needs. In addition, it seems clear that the high useful yields and high noise rejection of LSNMS techniques will prove useful for understanding many sputtering phenomena. The wide variety of instruments being tested at the present time are a clear indication that much work remains to be done to optimize these techniques.

Acknowledgement

This work was supported by the U.S. Department of Energy, BES-Materials Sciences, under Contract W-31-109-ENG-38.

References

1. Allen L, Boyd RW, Krazinski J, Malcuit MS, Stroud Jr. CR (1985). Laser intensity for maximum yield in multiphoton ionization. Phys. Rev. Lett. 54: 309-312.

2. Andersen HH, Bay HL (1981). Sputtering yield measurements. Topics in Appl. Phys. 47: 145-218. Springer, Berlin.

3. Bay HL (1987). Laser induced fluorescence as a technique for investigation of sputtering phenomena. Nucl. Instr. Meth. in Phys. res. 18:430-445.

4. Bay HL, Berres W, Hintz E (1982). Surface normal velocity distribution of sputtered Zr-atoms for light-ion irradiation. Nucl. Instr. Meth. 194: 555-559.

5. Becker CH, Gillen KT (1984a). Surface analysis by nonresonant multiphoton ionization of desorbed or sputtered species. Anal. Chem. 56: 1671-1674.

6. Becker CH, Gillen KT (1984b). Nonresonant multiphoton ionization as a sensitive detector of surface concentrations and evaporation rates. Appl. Phys. Lett. 45: 1063-1065.

7. Becker CH, Gillen KT (1985). Surface analysis of contaminated GaAs: comparison of new laser-based techniques with SIMS. J. Vac. Sci. Technol. A3: 1347-1349.

8. Becker CH, Gillen KT (1986). General post-ionization of sputtered and desorbed species by intense untuned radiation. In Secondary Ion Mass Spectrometry, SIMS V. Benninghoven A, Colton RJ, Simons DS, Werner HW (Eds.), 85-89, Springer, Berlin.

9. Betz G, Husinsky W (1986). Laser fluorescence studies of neutral particles sputtered from Cr, Cr_2O_3 and Cr_3C_2 targets. Nucl. Instrum. Meth. B15: 165-168.

10. Betz G, Wehner GK (1983). Sputtering of multicomponent materials. Sputtering by Particle Bombardment II, Behrisch R (Ed.), Topics in Applied Physics 52: 11-90, Springer, Berlin.

11. Biersack JP, Haggmark LG (1980). A Monte Carlo computer program for the transport of energetic ions in amorphous targets. Nucl. Instr. Meth. 174: 257-269.

12. Blackburn MB, Mermet JM, Boutilier GD, Winefordner JD (1979). Saturation in laser excited atomic fluorescence spectrometry: experimental verification. Appl. Opt. 18: 1804-1807.

13. Blum P (1977). Energy spectrum of Na sputtered from NaI measured with an optical spectrometer. In Proc. 7th Int. Vacuum Congress and 3rd Int. Conf. on Solid Surfaces. Dobroozemsky R, Rudenauer F, Viehbock FP, Breth A (Eds.), Institut fur Allgemeine Physik, TU Wien, Austria, 1469-1472.

14. Christie WH, Goeringer DE (1986). Small sample analysis using sputter atomization/resonance ionization mass spectrometry. In Resonance Ionization Spectroscopy. Hurst GS, C. Grey Morgan (Eds.), Inst. Phys. Conf. Ser. No. 84: 169-174.

15. Dullni E (1985). Laser fluorescence measurements of the flux density of titanium sputtered from an oxygen covered surface. Appl. Phys. A38: 131-138.

16. Gruen EM, Krauss AR, Pellin MJ (1985). Effects of monolayer coverages on substrate sputtering yields. Rad. Effects 89: 113-127.

17. Gruen DM, Pellin MJ, Young CE, Medelsohn MH, DeWald AB (1983). Outer shell excitation mechanisms and static mode laser fluorescence spectroscopy of sputtering atoms. Physica Scripta. T6: 42-53.

18. Haggmark LG, Biersack JP (1980). Monte Carlo calculations of light-ion sputtering as a function of the incident angle. J. Nucl. Mater. 93/94: 664-669.

19. Hammer D, Benes E, Blum P, Husinsky W (1976). Velocity spectrometer for particles in the 10-meV to 10-keV range. Rev. Sci. Instrum. 47: 1178-1182.

20. Herrmannsfeldt WB (1981). EGUN - the SLAC electron optics program. Report SLAC-226, UC-28 (A) Stanford Linear Accelerator Center, Stanford University, Stanford, CA.

21. Hintz E, Rusbolt D, Schweer B, Bohdansky J, Roth J, Martinelli AP (1980). The determination of the flux density of sputtered atoms by means of pulsed dye laser excited fluorescence. J. Nucl. Mater. 93&94: 656-663.

22. Husinsky W, Betz G, Girgis I (1983). Energy distribution of sputtered metastable Ca atoms. Phys. Rev. Lett. 50: 1689-1692.

23. Husinsky W, Betz G, Girgis I (1984). Ground state and excited state sputtering Doppler-shift laser-fluorescence studies of Cr and Ca targets. J. Vac. Sci. Technol. A2: 698-701.

24. Husinsky W, Betz G, Girgis I, Viehbock F, Bay HL (1984). Velocity distributions and sputtering yields of chromium atoms under argon, oxygen and carbon ion bombardment. J. Nucl. Mater. 128&129: 577-582.

25. Husinsky W, Bruckmuller R, Blum P (1980). Velocity measurements of sputtered particles using a laser-Doppler method. Nucl. Instrum. Meth. 170: 287-293.

26. Husinsky W, Bruckmuller R, Blum P, Viehbock F, Hammer D, Benes E (1977). Measurements of the velocity spectrum of sputtered Na from a NaI target by a Doppler shift laser spectrometer. J. Appl. Phys. 48: 4734-4740.

27. Husinsky W, Girgis I, Betz G (1985). Doppler shift laser fluorescence spectroscopy of sputtered and evaporated atoms under Ar^+ bombardment. J. Vac. Sci. Technol. B3: 1543-1545.

28. Husinsky W, Wurz P, Strehl B, Betz G (1987). Cr atoms sputtered from different matrices. Nucl. Instr. Methods B18: 452-457.

29. Kimock FM, Baxter JP, Pappas DL, Korbin PH, Winograd N (1984). Solids analysis using energetic ion bombardment and multiphoton resonance ionization with time-of-flight detection. Anal. Chem. 56: 2782-2791.

30. Kimock FM, Baxter JP, Winograd N (1983). Ion and neutral yields from ion bombarded metal surfaces during chemisorption using low dose SIMS and multiphoton resonance ionization. Surf. Sci. 124: L41-L48.

31. Kimock FM. Pappas DL, Wiongrad N (1985). Matrix effects on the electronic partitioning of iron atoms desorbed from surfaces by energetic ion bombardment. Anal. Chem. 57: 2669-2674.

32. Krauss AR, Wright RB (1980). Energy and mass distribution of sputtered particles. J. Nucl. Mater. 89: 229-252.

33. Landau LD, Lifshitz EM (1960). Integration of the equation of motion. Mechanics, Pergamon, Oxford, Ch. 3: 25-40.

34. Liebl H (1983). Combined electrostatic objective and emission lenses for microcharacterization of surfaces. Int. J. Mass Spectrom. Ion Phys. 46: 511-518.

35. Lipinsky D, Jede R, Ganschow O, Benninghoven A (1985). Performance of a new ion optics for quasisimultaneous secondary ion, secondary neutral, and residual gas mass spectrometry. J. Vac. Sci. Technol. A3: 2007-2017.

36. Matsunami N, Yamamura Y, Itikawa Y, Itoh N, Kazumata Y, Miyagawa S, Morita K, Shimizu R (1980). Energy dependence of sputtering yields of

monatomic solids. Institute of Plasma Physics, Nagoya, Japan, Report IPPJ-AM-14.

37. Oechsner H, Ruhe W, Stumpe E (1979). Comparative SNMS and SIMS studies of oxidized Ce and Gd. Surf. Sci. 85: 289-301.

38. Parks JE, Beekman DW, Moore LJ, Schmitt HW, Spaar MT, Taylor EH, Hutchinson JMR, Fairbanks Jr. WM (1986a). Progress in analysis by sputter initiated resonance ionization spectroscopy. In Resonance Ionization Spectroscopy, Hurst GS, C. Grey Morgan (Eds.), Inst. Phys. Conf. Ser. No 84, Bristol, U.K., 157-162.

39. Parks JE, Beekman DW, Moore LJ, Schmitt HW, Spaar MT, Taylor EH, Hutchinson JMR, Fairbanks Jr. WM (1986b). Progress in materials analysis using sputter initiated resonance ionization spectroscopy. 11th International Congress on X-ray Optics and Microanalysis, J.D. Brown and R.H. Packwood (Eds.), Univ. West. Ontario, London, Ontario, Canada, 425-429.

40. Parks JE, Schmitt HW, Hurst GS, Fairbanks Jr. WM (1983). Sputter-initiated resonance ionization spectroscopy. Thin Solid Films 108: 69-78.

41. Pellin MJ, Gruen DM, Young CE, Wiggins MD (1983). Electronic excitation of Ti atoms sputtered by energetic Ar^+ and He^+ from clean and monolayer oxygen covered surfaces. Nucl. Instr. Meth. 218: 771-776.

42. Pellin MJ, Wright RB, Gruen DM (1981). Laser fluorescence spectroscopy of sputtered zirconium atoms. J. Chem. Phys. 74: 6448-6457.

43. Pellin MJ, Young CE, Calaway WF, Burnett JW, Jørgensen B, Schweitzer EL, Gruen DM (1987). Sensitive low damage surface analysis using resonance ionization of sputtered atoms. Nucl. Instr. and Meth. B18: 446-451.

44. Pellin MJ, Young CE, Calaway WF, Gruen DM (1984). Trace surface analysis with pico-coulomb ion fluences: direct detection of multiphoton ionized iron atoms from iron-doped silicon targets. Surf. Sci. 144: 619-637.

45. Pellin MJ, Young CE, Calaway WF, Gruen DM. (1986). Trace surface analysis: 30 ppb analysis with removal of less than a monolayer. Nucl. Instr. and Meth. B13: 653-657.

46. Pellin MJ, Young CE, Gruen DM, Aratono Y, DeWald AB (1985). Oxygen underlayer formation of titanium by "static mode" laser fluorescence and Auger spectroscopy. Surf. Sci. 151: 477-502.

47. Pellin MJ, Young CE, Mendelsohn MH, Gruen DM, Wright RB, DeWald AB (1982). Oxygen and titanium sputtering yields as determined by laser fluorescence and Auger electron spectroscopy for monolayer oxygen coverage of polycrystalline Ti. J. Nucl. Mater. 111/112: 738-743.

48. Poschenrieder WP (1972). Multiple-focusing time-of-flight mass spectrometers. Part II. TOFMS with equal energy accceleration. Int. J. Mass Spectrom. Ion Phys. 9: 357-373.

49. Reuter W (1986). Post-ionization of sputtered particles: a brief review. Secondary Ion Mass Spectrometry, SIMS V. Benninghoven A, Colton RJ, Simons DS, Werner HW, (Eds.), 94-102, Springer, Berlin.

50. Sakurai T, Fujita Y, Matsuo T, Matsuda H, Katakuse I, Miseki K (1985). A new time-of-flight mass spectrometer. Int. J. Mass Spectrom. Ion Processes 66: 283-290.

51. Sakurai T, Matsuo T, Matsuda H (1985). Ion optics for time-of-flight mass spectrometers with multiple symmetry. Int. J. Mass Spectrom. Ion Processes 63: 273-287.

52. Schweer B, Bay HL (1980). Measurement of the population distribution of sputtered Fe-atoms with laser-induced fluorescence spectroscopy. In Proc. IVth Int. Con. on Surface Science. Degras DA, Costa M, (Eds.) Vide, Couches Minces. 1349-1352.

53. Schweer B, Bay HL (1982). On the velocity distribution of excited Fe-atoms by sputtering of iron. Appl. Phys. A29: 53-55.

54. Siegel MW, Vasile MJ (1981). New wide angle high transmission energy analyzer for secondary ion mass spectrometry. Rev. Sci. Instrum. 52: 1603-1615.

55. Sigmund P (1969). Theory of sputtering. I. Sputtering yield of amorphous and polycrystalline targets. Phys. Rev. 184: 383-416.

56. Sigmund P (1972). Collision theory of displacement damage. Rev. Roum. Phys. 17: 1079-1106.

57. Sigmund P (1977). Sputtering processes: collision cascades and spikes. In Inelastic Ion-Surface Collisions. Tolk NH, Tully JC, Heiland W, White CW (Eds.), 121-152, Academic Press, New York.

58. Thompson MW (1968). II. The energy spectrum of ejected atoms during the high energy sputtering of gold. Philos. Mag. 18: 377-414.

59. Winograd N, Baxter JP, Kimock FM (1982). Multiphoton resonance ionization of sputtered neutrals: a novel approach to material characterization. Chem. Phys. Lett. 88: 581-584.

60. Wright RB, Pellin MJ, Gruen DM (1981a). Velocity distribution of sputtered U atoms as determined by laser induced fluorescence spectroscopy. Nucl. Instr. Meth. 182&183: 167-178.

61. Wright RB, Pellin MJ, Gruen DM (1981b). Velocity distribution of sputtered Zr atoms as determined by laser induced fluorescence spectroscopy. Surf. Sci. 110: 151-178.

62. Wright RB, Pellin MJ, Gruen DM, Young CE (1980). Laser fluorescence spectroscopy of sputtered uranium atoms. Nucl. Instr. Meth. 170: 295-302.

63. Wright RB, Young CE, Pellin MJ, Gruen DM (1982). High resolution continuous wave laser induced fluorescence spectroscopy of sputtered Zr atoms. J. Vac. Sci. Tech. 20(3): 510-514.

64. Young CE, Calaway WF, Pellin MJ, Gruen DM (1984). Velocity and electronic state distributions of sputtered Fe atoms by laser-induced fluorescence spectroscopy. J. Vac. Sci. Tech. A2: 693-697.

65. Young CE, Pellin MJ, Calaway WF, Jørgensen B, Schweitzer EL, Gruen DM (1987a). Trace surface analysis via RIS/TOF mass spectrometry. Inst. Phys. Conf. Ser. No. 84: Section 4, 163-168.

66. Young CE, Pellin MJ, Calaway WF, Jorgensen B, Schweitzer EL, Gruen DM (1987b). Laser-based secondary neutral mass spectroscopy: useful yield and sensitivity. Nucl. Instr. Meth. B27: 119-129.

67. Zare RN (1984). Laser chemical analysis. Science 226: 289-303.

Discussion with Reviewers

J.E. Parks: The laser volume used in the analysis of the fraction of sputtered atoms in the photoionization volume is a cylinder of height (z_2-z_1) and radius h, and its orientation is such that the axis of the cylinder is perpendicular, or normal to the surface of the sample. How realistic is this volume and orientation used in the analysis to the actual measurement volume and orientation of the laser beam? What is the geometry of the laser beam and what is its orientation with respect to the sample?
Authors: The laser region of interest for laser-based sputtered neutral mass spectrometry is the intersection of (1) the laser-illuminated volume in front of the target and (2) photoion extraction volume defined by the ion optic detection system. For simple extraction and detection systems, such as those used in TOF systems, (2) can be well represented as having cylindrical symmetry. Thus, the chosen volume is realistic in those cases that the laser light completely illuminates this volume. For more complicated extraction geometries, such as those involving magnetic sector instruments, which have single axis focal properties, the treatment in the paper can be easily extended to more elliptical geometries.

J.E. Parks: In connection with SARISA EARTOF, is the energy spread of the extracted photoions 1000 eV with an uncertainty of 100 eV or is the spread just 100 eV with a mean energy of 1000 eV? What is the 152 eV energy spread mentioned for the conditions of Fig. 10?
Authors: The energy spread is 1000 eV $\pm$ 100 eV for a linear extraction ramp. The 152 eV energy spread, which is centered about 1000 eV, is determined from a complete calculation of the cylindrically symmetric potential fields of the SARISA apparatus.

J.E. Parks: What explanation can be offered for the discrepancy between the 17% value for the calculated yield and the 9% value for the measured yield?
Authors: The discrepancy could well be due to slight misalignments in the rather complicated EAR-TOF beam line. Another possibility is discussed in response to the second question of Dr. H. Liebl.

J.E. Parks: What is the distinction between MPI (multiphoton ionization) and RIS (resonance ionization spectroscopy) as they are used in this paper?
Authors: MPI is used here to represent ionization in the absence of intermediate resonances. In practice, MPI refers to using the laser as a nonspecific ionization source. RIS refers to using the resonances of a particular atomic or molecular species to selectively ionize that component of the sputtered flux.

J.E. Parks: Does the 5% measured yield correspond to a 2 μA current in a 2 μs pulse? If not, what yield would be measured with 2 μA peak current in a 2 μs pulse?
Authors: 5% refers to a 2 μA peak current, 2 μs pulse of primary ions.

H. Liebl: In the raytracing plot (Fig. 8), the photoions appear to start from the sample surface while the photoionization takes place some distance away. What are the starting conditions (axial distance, energy, angles) on this plot?

Authors: The raytracing plot in Fig. 8 does indeed start at the sample. The neutral sputtered atoms leave the target midpoint with 3 eV of kinetic energy and a $\pm$ 60° range of angles about the target normal. The neutrals are assumed to be instantaneously converted to photoions at t = 500 nsec following the delta function primary ion pulse. Similar studies have been made for secondary neutral atoms ranging in energy from 1 to 10 eV with a wide range of laser ionization delay times. The results are similar and too complicated to display in just one figure.

H. Liebl: How is the secondary beam affected by the primary beam turning plates (Fig. 7)?
Authors: The primary beam turning plates are made up of three elements as shown in Fig. 7. The outermost plate, the first crossed by the primary ion beam on its way to the target, is fixed at ~ -1000 V. The second plate is slotted to allow passage of the primary ions and is pulsed from ~ -300 V to ~ 0 V following passage of the primary ion pulse. Similarly, the third solid plate is pulsed from 300 V to ~ 0 V. The secondary photoions see some field leakage of the -1000 V through the slot of the second plate. The deflection caused by this situation is corrected by inducing a slight angle in the photoions in the horizontal deflection plates closest to the sample surface. This is undesirable and causes some loss of transmission. In a new system presently under construction, this is corrected by pulsing the first plate to 0 V as well.

C. Becker: For Fig. 6, what is the approximate range of absolute values of the laser power density? Is this laser beam focused; if so, to what diameter? It may be noted that increases in signal are indeed possible after reaching saturation of MPI for focused laser beams because the effective focus volume continues to expand, at least until a detector viewing factor cuts it off.
Authors: The range of intensities shown are 0.3 x 10^7 watts/cm^2. The laser was collimated and apertured to a 1 mm x 3 mm cross-section beam. The aperturing of the beam effectively eliminated beam volume effects. The choice of this relatively large laser volume may not be optimum for all experiments. The fraction of sputtered atoms in the laser volume is certainly large for large volumes. Unfortunately, the attainable laser intensity, and therefore, the fraction ionized, will be low however.

C. Becker: Were any nonstainless steel components used for the ion optics or did you need to take any other precautions to avoid sources to an iron background due to back-sputtering onto the sample?
Authors: The measurement of Fe required that all components which could potentially be exposed to the primary ion beam had to be gold plated. This reduced any sample contamination of iron to acceptable levels.

C. Becker: The authors remark that the detection limit for ^{56}Fe in the Si matrix is limited by nonresonant MPI of Si_2. I offer another possible explanation for the near-surface peak in concentration in Fig. 12: suppose this region, which likely embodies the native oxide, produces upon sputtering a significant yield of metastable Si_2 or Si_xO_y, which yields Si_2^+ with laser irradiation. The lower signal at the

surface (the first data point) would be caused by surface contamination of the sample. Measuring the ratio of m/z 54/56 in this region would be informative. What is your opinion?

Authors: Clearly the proper statement is that laser generated Si_2^+ limits the detectable ^{56}Fe. The relative closeness of the Si_2 neutral absorption lines leads us to suspect Si_2 as the culprit. Other possible sources need also to be considered. We are presently measuring the 54/56 ratios as a function of depth. This is an excellent suggestion.

C. Becker: Numerous atomic species have their lowest-lying excited states and their ionization potentials at energies considerably higher than for metal atoms such as Fe, notably elements with lower atomic number. Strategies for their ionization often require two or three photons for the transition to an excited state and/or the ionization continuum, with associated higher laser beam power densities required to maintain efficient ionization. Higher power densities typically mean that focusing is needed so that somewhat smaller collection volumes result. In addition, higher power densities typically mean that the selectivity over nonresonant MPI processes decreases. Do you agree with this evaluation?

Authors: Excitation of the lighter atomic species with conventional laser sources often requires a two-photon excitation to the first resonant level. The higher laser intensities required to saturate these transitions will lead to a loss of selectivity in the laser ionization process due to line broadening effects. An analysis of the noise due to nonresonant ionization in this case requires a precise definition of the various species present on the sample surface. Atomic gas phase absorption lines are extremely sharp and the possibility of accidental overlap even with power broadening remains small (but not zero). Additional resonant enhancement can be obtained by using a tunable photon in place of our excimer laser. Substantial resonances exist in the so-called ionization continuum.